HOKKAIDO UNIVERSITY

Title	The Umov effect for single irregularly shaped particles with sizes comparable with wavelength
Author(s)	Zubko, Evgenij; Videen, Gorden; Shkuratov, Yuriy et al.
Citation	Icarus, 212(1), 403-415 https://doi.org/10.1016/j.icarus.2010.12.012
Issue Date	2011-03
Doc URL	https://hdl.handle.net/2115/45038
Type	journal article
File Information	Ica212-1_403-415.pdf

Hokkaido University Collection of Scholarly and Academic Papers : HUSCAP

The Umov Effect for Single Irregularly Shaped Particles with Sizes Comparable with Wavelength

Evgenij Zubko,[1,2] Gorden Videen[3], Yuriy Shkuratov,[2] Karri Muinonen,[1,4] Tetsuo Yamamoto[5]

[1] *Department of Physics, PO. Box 64, FI-00014 University of Helsinki, Finland*

[2] *Institute of Astronomy, Kharkov National University, Sumskaya St. 35, Kharkov, 61022, Ukraine*

[3] *Space Science Institute, 4750 Walnut Street, Suite 205, Boulder, CO 80301 USA*

[4] *Finnish Geodetic Institute, PO. Box 15, FI-02431 Masala, Finland*

[5] *Institute of Low Temperature Science, Hokkaido University, Kita-ku North 19 West 8, Sapporo 060-0819, Japan*

Abstract. The Umov effect manifests itself as an inverse correlation between the linear polarization maximum of an object's scattered light P_{max} and its geometric albedo A. This effect is observed for the Moon, Mercury and Mars, and there are data suggesting this effect is valid for asteroids. The Umov effect is due to the contribution of interparticle multiple scattering that increases albedo and decreases polarization. We here study if the Umov effect can be extended to the case of single irregularly shaped particles with sizes comparable with the wavelength. This, in particular, is important for cometary dust polarimetry. We show the Umov effect being valid for weakly absorbing irregular particles ($\mathrm{Im}(m) \leq 0.02$) almost through the entire range of size parameters x considered. Highly absorbing particles ($\mathrm{Im}(m)>0.02$) follow the Umov effect only if x exceeds 14. In the case of weakly absorbing particles, the inverse correlation is essentially non-linear, which is caused by the contribution of particles with small x. However, averaging over many different types of irregularly shaped particles could make it significantly more linear. The size averaging does not change qualitatively the diagram $\log(P_{max}) - \log(A)$ for weakly absorbing particles. For single irregular particles whose sizes are comparable with wavelength, there is no reliable correlation between the slope of the polarization curve h near the inversion phase angle and geometrical albedo A. Using the extended Umov law, we estimate the geometric albedo of dust particles forming cometary circumnuclear haloes $A = 0.1 - 0.2$, which is a few times larger than the average geometric albedo over the entire comae. Note that, using the obtained values for A of cometary particles, one can derive their number density in circumnuclear haloes from photometric observations.

Keywords: Umov effect, light scattering, cometary dust particles, discrete dipole approximation.

1. Introduction

The inverse correlation between geometric albedo and polarization degree of light scattered from rough surfaces illuminated by unpolarized light was noted more than 150 years ago by Provostaye and Desain (1852). They also found depolarization of light scattered from the surfaces illuminated by linearly polarized light: the depolarization is higher for bright rough surfaces. Much later Nikolay Umov (1905) described the interrelation between geometric albedo and depolarization for colored media that scatter light diffusively. Although in the original manuscript Umov provided only a qualitative description of measurements, since then the inverse correlation between the surface brightness and degree of linear polarization has been referred to as the Umov effect or Umov Law (see, e.g., Toporets, 1950; Dollfus et al., 1971; Wolff, 1980; Woessner and Hapke, 1987; Shkuratov and Opanasenko, 1992; Hapke, 1993; Levasseur-Regourd et al., 1997; Hadamcik et al., 2002; Penttilä et al., 2003; Mishchenko et al., 2007; Shkuratov et al., 2007; Zubko et al., 2009a). Note also that Lyot (1929) noticed a dramatic difference in linear polarization of the first and last quarters of the Moon, which have substantially different albedo.

Quantitative data on the effect have been derived by astronomers observing the Moon (e.g., Pellicori, 1969; Dollfus and Bowell, 1971; Shkuratov, 1981; Kornienko et al., 1982; Novikov et al., 1982; Shkuratov and Opanasenko, 1992). Clark (1965) assumed a linear relationship between the maximum of positive polarization and geometric albedo A, though a year earlier Avramchuk (1964) found a more adequate fitting function for the lunar data: a linear dependence between the logarithms of geometric albedo and the maximum of linear polarization. We emphasize that applying the logarithmic scales is reasonable, since the effect is related to the linear polarization degree P. Indeed,

$$P = \frac{I_\perp - I_\parallel}{I_\perp + I_\parallel}, \tag{1}$$

where $I_\perp$ and $I_\parallel$ denote the intensities of the scattered light components that are perpendicular and parallel to the scattering plane, respectively. Note that the scattering plane is defined by the location of the Sun, target, and observation point. The value P is a complicated function of phase angle α. Evidently, the value $(I_\perp + I_\parallel)$ is proportional to albedo A. Therefore, if the difference $(I_\perp - I_\parallel)$ does not depend on albedo, then one can state the relationship: log$P$ + log$A$ = const. However, the value $(I_\perp - I_\parallel)$ can be a complicated function of albedo and other parameters, and, as a consequence, the relationship is not trivial.

Figure 1 shows the correlation between the logarithm of albedo A and the logarithm of the maximum of positive polarization P_{max} for 22 sites on the Moon (the data are adapted from Shkuratov et al., 1992). For this diagram we used the discrete telescope polarimetric measurements that were carried out in red (0.65 μm) and blue (0.42 μm) light. Shkuratov et al. (1992) used albedo A at $\alpha = 3.1°$, and they approximated P_{max} by the polarization degree at $\alpha = 90°$. Note that, strictly speaking, the geometric albedo is defined at $\alpha = 0°$ (e.g., Karttunen et al., 1996). However, in ground-based observations of the Moon, the regime of exact backscattering cannot be achieved; therefore, geometric albedo was approximated by albedo at $\alpha = 3.1°$. As one can see in Fig. 1, the inverse correlation between $\log(P_{max})$ and $\log(A)$ is very strong. Nevertheless, there are deviations from the regression line that contain information about the properties of the target (Shkuratov, 1981; Kornienko et al., 1982; Novikov et al., 1982; Shkuratov and Opanasenko, 1992; Dollfus, 1998).

The physical mechanism governing the Umov effect is quite clear: in a bright regolith-like surface, multiple scattering between particles is highly pronounced; i.e., light interacts with many particles before being completely absorbed or leaving the discrete medium. Multiple scattering occurs between particles that are not located in one plane, which means that the scattering plane changes at every scattering event. In terms of the Stokes parameters describing the scattered light (e.g., Bohren and Huffman, 1983), this leads to a "distribution of polarization state" between the three Stokes parameters Q, U, and V. However, in the standard geometry of light scattering, i.e. when the surface is either illuminated or observed along the surface normal, the averaging over many paths of light in a discrete disordered medium reduces the last two parameters due to isotropy of the medium. The scattered light therefore becomes less polarized.

The influence of multiple scattering on positive polarization has been studied in the geometric optics approximation with numerical simulation of light scattering in powdered surfaces (Wolff, 1980; Shkuratov and Grynko, 2005). In particular, it was shown that powders consisting of particles with different shapes demonstrate the different $P_{max} - A$ dependences (Shkuratov and Grynko, 2005). It also was clearly demonstrated that the diagram $\log(P_{max}) - \log(A)$ can be non-linear, especially, in the case of dark surfaces (Wolff, 1980).

When the surface is illuminated or observed along the surface normal, the polarization degree is zero at the exact backscattering. At phase angles from opposition to approximately 30°, the polarization degree may be negative, and this portion of the polarization phase function often is referred to as the negative polarization branch (NPB). The NPB ends at the inversion phase angle α_{inv} where the positive polarization branch begins. The polarization continues to the polarization maximum P_{max} occurring at a phase angle typically larger than 90° (see, e.g.,

Dollfus and Bowell, 1971; Dollfus et al., 1971; Dollfus and Titulaer, 1971). The Umov effect is most often applied to polarization degree near P_{max}. Sometimes, it has been discussed in the context of the NPB (Shkuratov et al., 1992; Shkuratov and Opanasenko, 1994; Shkuratov et al., 1994; Zellner et al., 1974). While this may not be inconsistent with the very general original qualitative description provided by Umov (1905), we know that the mechanisms that produce the negative and positive polarization that manifest themselves in the two different branches are different (e.g., Shkuratov et al., 1994; Zubko et al., 2008; Tyynelä et al., 2010).

One interesting consequence of the Umov effect is to link the slope h of the polarization curve at the inversion phase angle α_{inv} to the geometric albedo A (e.g., Zellner et al., 1977a,b; Geake and Dollfus, 1986; Wolff, 1980; Shkuratov 1980; Shkuratov et al., 1992). The correlation between h and A is widely used to determine albedo of asteroids (e.g., Lupishko and Mohamed, 1996; Cellino et al., 1999; 2005). Obviously, the slope h of the polarization includes information not only about the amplitude of P_{max}, but also about the location and value of the NPB minimum. The correlation between P_{max} and h is not linear for the Moon. (Dollfus and Bowell, 1971; Opanasenko and Shkuratov 1994).

The NPB does not depend on albedo as simply as the positive polarization. For instance, the lunar diagram $P_{min} - A$ has a horse-shoe shape (Shkuratov et al., 1992; Opanasenko and Shkuratov, 1994), and the same behavior was found for many samples in laboratory measurements (Shkuratov et al., 1994). Different measurements also have shown that the shape and amplitude of the NPB strongly depend on the structure and size of particles and, in some cases, the NPB may not exist (e.g., Shkuratov et al., 2002, Ovcharenko et al., 2006). The same complex behavior of the NPB has been observed in numerical simulations of light scattering by single irregularly shaped particles (e.g., Zubko et al., 2006). While the parameter h that depends on the NPB is useful, it is physically intractable. No wonder that, when some object produces a NPB different from what is considered to be typical, like the nucleus of comet 2P/Encke, the relationship between the geometric albedo and the slope of the polarization curve fails (Boehnhardt et al., 2008). Note also that the inverse correlation between the slope of the polarization curve and geometrical albedo fails for very dark surfaces when the contribution of multiple scattering is weak (Hapke, 1993; Shkuratov 1980; Zellner et al., 1977a,b). Note that recent infrared studies for the geometric albedo of asteroids have renewed interest in independent examination of the obtained results; which can be done using the slope of the polarization curve h (e.g., Harris et al., 2007).

In this paper, we focus on the Umov effect and its formulation as an inverse correlation between albedo and P_{max} in application to single dust particles having sizes comparable with the

wavelength. In section 2, we introduce briefly the discrete dipole approximation (DDA) – a flexible technique to perform numerical simulations of light scattering by particles of arbitrary shapes and internal structures and, also, our methods of generation of sample particles. In section 3 we present and discuss results. Finally, in section 4 we present the conclusions of this research.

2. Modeling light scattering

2.1. The discrete dipole approximation (DDA) method

We compute light scattering by irregularly shaped particles whose sizes are comparable with the wavelength of the incident light using the DDA (e.g., Purcell and Pennypacker, 1973; Draine, 1988; Draine and Flatau, 1994; Yurkin and Hoekstra, 2007; Zubko et al., 2010). This approach allows us to consider particles with arbitrary shape and internal composition. In the DDA, a target particle is modeled with an array of small constituent volumes that together reproduce the shape and internal optical properties of the original particles. These constituent volumes must be significantly smaller than the wavelength of the incident electromagnetic wave, and their scattering properties take the form of a simple analytic expression (i.e., the Rayleigh approximation). With this replacement, one can reduce the light-scattering problem to a system of linear algebraic equations. One additional restriction is that they are located in a regular cubic lattice, so that an FFT may be used to accelerate the computations (Goodman et al., 1991). We use a well tested implementation of the DDA to perform the calculations of this manuscript (Penttilä et al., 2007).

An important parameter specifying the DDA applicability is the size of the cubic lattice spacing d. In application to irregular particles, the DDA provides accurate numerical results under the condition $kd|m| \leq 1$, where wavenumber $k = 2\pi/\lambda$, λ is the wavelength of the incident electromagnetic wave, and m is the refractive index of particle (Zubko et al., 2010). Note that throughout this study, the parameter $kd|m|$ remains less than 0.85.

2.2. Models of irregularly shaped particles

We study six types of irregularly shaped particles that could be labeled as follows: agglomerated debris particles, pocked spheres, rough-surface spheres, strongly damaged spheres, debris of spheres, and Gaussian random particles. Example images of these particles are shown in Fig. 2. One can see that all particles appear to be essentially non-spherical and reveal a wide variety of particle structures. Indeed, there are highly compact structures, such as rough-surface spheres and Gaussian random particles. Fluffy structure is represented by agglomerated debris

particles and pocked spheres. While strongly damaged spheres and debris of spheres correspond to moderate cases.

Except for the Gaussian random particles, irregularly shaped particles have been generated using one algorithm, which is as follows. In computer memory, a spherical volume is filled with a regular cubic lattice that is considered as the initial matrix of the irregular particles. In the general case, we consider two sizes for the initial matrix, consisting of 137,376 and 1,099,136 cells; whereas, the choice between them is based on the requirement of the validity criterion for the DDA (i.e. $kd|m| < 0.85$). In the process, the elements of the cubic lattice inside the initial matrix are assigned material properties corresponding to the refractive indices of the particles. All cubic cells forming this initial matrix are divided into two groups: cells belonging to the surface layer and cells internal to the surface layer. The depth of the surface layer is a parameter of our model. For instance, in the case of agglomerated debris particles and rough-surface spheres, the depth takes value of only 0.5% of the radius of the initial matrix, i.e., the surface layer is formed only by dipoles having direct contact with the surrounding empty space. In the case of pocked spheres, the depth is 12.5% of the radius of the initial matrix. Strongly damaged spheres and debris of spheres are generated having no surface layer; i.e., all cells of the initial matrix are treated as internal.

Once cells forming the initial matrix are divided into two sub-groups, we choose seed cells for empty space and material at random. In general, we distinguish two types of seed cells for empty space, those belonging to surface layer and those belonging to the internal volume; whereas, seed cells for the material are allocated only among internal cells. For instance, agglomerated debris particles are generated with 100 seed cells of empty space randomly chosen in the surface layer, 20 seed cells of empty space, and 21 seed cells of material randomly allocated throughout the internal volume. For rough-surface spheres, the numbers of seed cells are 1200 for empty space in the surface layer, 150 for material and 0 for empty space within the interior. In the case of pocked spheres they are 100, 50, and 0, respectively. Because strongly damaged spheres and debris of spheres are generated with zero depth of the surface layer, it implies that the number of seed cells for empty space allocated in the surface layer is 0. For strongly damaged spheres, there are 20 seed cells of empty space and 21 seed cells of a material; whereas, for debris of spheres the numbers of seed cells of empty space and material are both equal to 4.

The final stage of generating a target particle is to evaluate the rest of the cells forming the initial matrix: step-by-step, each cell distinct from the seed cells is marked with the same optical properties as that of the nearest seed cell. More images, volume distributions, and light-

scattering properties of agglomerated debris particles, pocked spheres, rough-surface spheres, and strongly damaged spheres can be found in Zubko et al. (2006; 2009a).

Using the algorithm described in Muinonen et al. (1996), we have generated a set of 100 samples of random Gaussian particles. This type of particle is parameterized by the relative radius standard deviation σ and power law index in the covariance function of the logarithmic radius ν, which take values of 0.245 and 4, respectively. Unlike other types of irregular particles involved in this study, random Gaussian particles possess a smooth surface; nevertheless, their shape is significantly non-spherical. Note that light scattering by exactly the same ensemble of shapes of random Gaussian particles has been studied in Zubko et al. (2007), and additional images of sample particles can be found therein.

Two important parameters characterizing irregularly shaped particles are the radius of the circumscribing sphere r_{cs} and the packing density ρ of the particle material. Note that these parameters do not describe completely the properties of a particle. The more complicated the structure, the more parameters are needed to describe it. Nevertheless, even considering the effects of varying these two parameters may significantly improve our understanding of scattering peculiarities of irregularly shaped particles. In cases of non-Gaussian irregular particles, the radius of the circumscribing sphere is close to the radius of the initial matrix; the difference does not exceed 1%. We approximate the circumscribing sphere with the largest sample from the set of 100 particles to preserve the size distribution of random Gaussian particles obtained with original algorithm described by Muinonen et al. (1996). We define the packing density of a particle as the ratio of volume occupied by the particle material to volume of the circumscribing sphere. Values of packing density are approximately 0.236 for agglomerated debris particles, 0.336 for pocked spheres, 0.523 for rough-surface spheres, 0.512 for strongly damaged spheres, 0.500 for debris of spheres, and 0.139 for random Gaussian particles. As one can see, the packing density varies over a wide range for the 6 types of irregularly shaped particles considered.

2.3. Parameters of particles

In general, light scattering by a small particle is determined primarily by the complex refractive index m of the particle material and the ratio of the particle size expressed as r_{cs} to the wavelength λ: $x = 2\pi\, r_{cs}\, /\lambda$ (e.g., Bohren and Huffman, 1983). While we use the radius of circumscribing sphere r_{cs} to express particle size, another parameter used is the radius of an

equal-volume sphere r_{eq}. We denote the size parameter of the equal-volume sphere as x_{eq} and note that x_{eq} can be derived from x and packing density ρ as follows: $x_{eq} = \rho^{1/3} x$.

Among the six types of irregularly shaped particles used in this study, we consider agglomerated debris particles as a realistic model for cosmic dust. Indeed, this type of particle meets two important features of cosmic dust, that being highly irregular and fluffy. To some extent, appropriateness of agglomerated debris particles has been confirmed recently in cometary applications. For instance, as has been shown in Zubko et al. (2009a), the degree of linear polarization produced by this type of irregular particles is consistent with polarimetric observations of cometary circumnuclear haloes. Besides, using agglomerated debris particles, it is possible to interpret quantitatively the polarimetric observations of the mega-outburst of comet 17P/Holmes in October of 2007 (Zubko et al. 2009b). Therefore, we study agglomerated debris particles in the most detail; whereas, the other five types of irregularly shaped particles are used for comparative analysis.

We consider agglomerated debris particles having 15 different refractive indices m, which are representative of materials in cometary dust and planetary regoliths. The actual values of refractive indices studied are given in Table 1. We classify these materials into two groups for convenience: highly absorbing, $\mathrm{Im}(m) > 0.02$, and weakly absorbing, $\mathrm{Im}(m) \leq 0.02$, materials.

Some of the listed refractive indices are artificial for cosmic dust applications, e.g., $1.2 + 0i$; nevertheless, there is an interest in considering how the scattering properties behave in such limits. The most commonly used models for cometary dust particles are so-called Ballistic Cluster-Cluster Aggregate (BCCA) and Ballistic Particle-Cluster Aggregate (BPCA) (e.g., Kimura, 2001; Kimura et al., 2008; Lasue et al., 2009). The distinctive feature for these aggregates is an extremely fluffy internal structure. Although BPCA is more compact than BCCA, both are much fluffier than agglomerated debris particles. However, within the effective medium approximation (e.g., Bohren and Huffman, 1983), agglomerated debris particles with $m = 1.2 + 0i$ could be considered as a rough model for silicate particles, but with significantly higher porosity. Note that the effective medium theory is widely used for an approximate incorporation of the porosity into simulation of light scattering by cometary dust particles. For instance, using such an approach, Grynko et al. (2004) fitted the phase function of comet 96P/Machholz 1 with the refractive index $m = 1.2 + 0.004i$.

Refractive index $m = 1.313 + 0i$ corresponds to pure water ice in visible (Warren, 1984). Refractive indices with real part $\mathrm{Re}(m) = 1.6$ and imaginary part $\mathrm{Im}(m)$ varying from 0.01 to $0.1i$, are consistent with organic material kerogen type II in visible (Khare *et al*., 1990). Note also that the refractive index $m = 1.6 + 0.02i$ can be associated as well with ice tholin in blue light (Khare

et al., 1993). Refractive index $m = 1.5 + 0.1i$ is a model for so-called "yellow stuff"(Jenniskens, 1993); whereas, $m = 1.7 + 0.1i$ corresponds to organic material studied by Pollack et al. (1994). The refractive index $m = 1.6 + 0.0005i$ is approximately Mg-rich pyroxene glass and $m = 1.758 + 0.0844i$ corresponds to iron-rich pyroxene glass in visible (Dorschner *et al*., 1995).

For agglomerated debris particles, the size parameter varies over a wide range. For all refractive indices, the smallest value of x is 2; whereas, the largest value depends on refractive index m. In most cases, the size parameter is varied in steps of either 1 or 2. Table 1 shows the values of x considered in this study.

Irregular particles other than agglomerated debris have been investigated at three different refractive indices $m = 1.313 + 0i$, $1.5 + 0.1i$, and $1.6 + 0.0005i$. In all these cases, x is varied from 2 to 14 with a fixed step of 2. Note that agglomerated debris particles also have been studied in the given set of m and x.

2.4. Averaging of light-scattering properties

Light-scattering properties of irregularly shaped particles are averaged over sample shape and orientation at each set of m and x. In all cases, except those of random Gaussian particles, we consider a minimum of 500 sample particle shapes. Light scattering by each sample particle has been computed for one random orientation of the incident electromagnetic wave and averaged over 100 scattering planes evenly distributed around the propagation direction of the incident light. This averaging over scattering planes does not require significant computational efforts; however, it improves significantly the statistical reliability of numerical results. We continue averaging over particle shape while fluctuations of the standard deviation of the degree of linear polarization over the entire range of phase angle α exceed 1%; therefore, the actual number of sample particles considered very often exceeds 500. More detail on averaging over scattering planes and control of the averaging quality can be found in Zubko et al. (2008).

For the random Gaussian particles, we consider a set of 100 sample particles. Therefore, in order to achieve a desirable accuracy in the averaging, we calculate the light scattering from each sample particle at different orientations with respect to the incident light. The minimum number of orientations is 5 per sample particle. Although the criterion for termination of the averaging process is the same as for non-Gaussian irregular particles, there is a significant difference: when a given number of orientations of random Gaussian particles does not provide a desirable accuracy of the averaging, we add one additional random orientation for each sample particle from the ensemble and only then check the accuracy again. Therefore, at the termination

of the averaging process, light-scattering properties of each sample particle are averaged over the same number of random orientations.

It should be emphasized that while many of the irregularly shaped particles considered in this manuscript have been already studied in Zubko et al. (2006; 2007; 2009a), the number of parameter sets here is significantly extended. For instance, in Zubko et al. (2006), agglomerated debris particles have been studied at 5 different refractive indices versus 15 in the current manuscript. The size parameter x previously did not exceed 16; whereas, in this manuscript it has been extended up to 26 or more at ten different refractive indices. In addition, we have significantly improved the quality of the averaging, so the present results are more statistically reliable. For instance, the minimum number of sample particles used in Zubko et al. (2006) was 200; whereas, here it is 500.

3. Results and discussion

3.1. Considering single-scattering and geometric albedo

When extending the Umov effect for the case of single particles comparable with the wavelength, the choice between single-scattering albedo ω and geometric albedo A plays an important role. The definitions for these types of albedo are as follows (Bohren and Huffman, 1983; Hanner et al., 1981):

$$\omega = C_{sca} / C_{ext}; \tag{2}$$

$$A = \pi S_{11}(0) / (k^2 G). \tag{3}$$

Here, C_{sca} and C_{ext} denote scattering and extinction cross-sections (Bohren and Huffman, 1983), respectively; $S_{11}(0)$ is the corresponding element of the Mueller matrix at $\alpha = 0°$; k is the wavenumber; and G is the geometric cross-section of the particle. Note that the result of the product (k^2 G) is dimensionless. Therefore, for simplicity, one can set $k = 1$ and measure the geometric cross-section of particles G in units of kd, where, d is the size of cells forming the cubic lattice. Formulae (2) and (3) show that for single particles there is a fundamental difference between ω and A. Indeed, the single-scattering albedo incorporates the intensity of light scattered in the entire space surrounding a target particle; whereas, the geometric albedo depends only on backscattering intensity. In other words, the geometric albedo defined for single particles equates to their backscattering efficiency; whereas, for regolith, the geometric albedo is a function of the single-scattering albedo due to multiple scattering. Note that the geometric albedo of a regolith

also depends on the phase function of its constituent particles (i.e., their angular profile of intensity normalized to their scattering cross section).

From a general point of view, the choice of single-scattering albedo for single particles seems to be more reasonable, since it includes the integral scattering, not scattering at an arbitrary phase angle. Such an assumption is consistent with the conclusion in Zubko et al. (2009a), where it was found that the positive polarization degree inversely correlates with the single-scattering albedo over a visibly wider range of Im(m). On the other hand, the use of single-scattering albedo meets an obvious difficulty when non-absorbing particles are considered. Indeed, at Im(m) = 0 the single-scattering albedo equals 1 through the entire range of size parameter x; whereas the positive polarization degree strongly varies with x (see, e.g., Asano and Sato, 1980; Zubko et al., 2006; 2007; 2009a). The use of the geometric albedo does not suffer this dilemma.

In order to consider the two types of albedo of which the Umov effect might refer, we present Fig. 3. The upper row of this figure shows the diagram of $\log(P_{\max})$ vs. $\log(\omega)$, and the bottom row shows the diagram of $\log(P_{\max})$ vs. $\log(A)$. All points in Fig. 3 represent agglomerated debris particles only and Table 1 summarizes the input parameters used in the computations. We formally define the maximum of positive polarization $P_{\max}$ for the range of phase angles α = 0–135°. This limitation is used to exclude the influence of the relatively strong positive polarization appearing near the forward scattering of irregular particles with compact structure and high refractive index (e.g., Zubko et al., 2006). In Fig. 3 the data points corresponding to different refractive indices are shown with various types of symbols (see legend). In both rows of Fig. 3, the left panel corresponds to highly absorbing materials, and the right panel corresponds to weakly absorbing materials. Arrowed lines in the bottom panels show schematically the dependence on size parameter x. Fig. 3 reveals a much stronger inverse correlation $P_{\max}$ with the geometric albedo A than with the single-scattering albedo ω, especially with respect to the weakly absorbing particles (right bottom panel). The relationship depends on the particle size, and only for weakly absorbing particles is there a functional dependence of $P_{\max}$ on A. No functional dependence appears between $P_{\max}$ and ω. Thus, one can conclude that the Umov effect for single particles appears only when considering the geometric albedo A rather than the single-scattering albedo ω. Therefore, in what follows, we consider and discuss the inverse correlation of $P_{\max}$ with A.

3.2. Non-linear inverse correlation in the diagram $\log(P_{max}) - \log(A)$

The arrows in the lower panels of Fig. 3 show the paths on the diagram taken when size parameter x increases. The shape of such lines is more complicated for highly absorbing particles due to there being an inflection point. Note that a similar inflection can be seen also for Im(m) = 0.02 on the right bottom panel in Fig. 3, which formally corresponds to weakly absorbing particles. The inflection point strongly depends on the imaginary part of the refractive index Im(m). For instance, in the case of Im(m) = 0.1 it occurs at $x \approx 4$–6; in the case of Im(m) = 0.05 it occurs at $x \approx 10$; and in the case of Im(m) = 0.02, it occurs at $x \approx 12$–16. An increase of the real part of refractive index Re(m) tends to shift the inflection point toward larger x, although such a tendency does not always occur. If the size parameter x exceeds the value corresponding to the inflection point, then a variation of x causes greater dispersion of data points through the $\log(P_{\max}) - \log(A)$ diagram.

Weakly absorbing particles produce non-linearity on the $\log(P_{\max}) - \log(A)$ diagram due to the contribution of very small particles, especially those for which x = 2–4. These small particles have an angular profile of the degree of linear polarization similar to Rayleigh particles, i.e., the polarization curve has a bell-like shape with rather high maximum of polarization, which is located near phase angle of 90 degrees. However, the linear polarization of Rayleigh particles does not depend on refractive index m at all; whereas, the intensity of backscattering and, hence, the geometric albedo A, obviously show significant variations with m (e.g., Bohren and Huffman, 1983).

Thus, for both weakly and highly absorbing particles non-linear regions on the $\log(P_{\max}) - \log(A)$ diagram are caused mainly by the contribution of the small particles. To illustrate this, we limit the data presented in the bottom panels in Fig. 3 using the condition $x \geq 14$ and show the results in the upper row of Fig. 4. As before, the left panel corresponds to highly absorbing particles, and the right panel corresponds to weakly absorbing particles. In Fig. 4, one can see that the distribution of points on the diagrams becomes visibly more regular and linear in comparison with that shown in bottom panels of Fig. 3.

Interestingly, when considering irregular particles with fixed size parameter x = 14 (see bottom panels in Fig. 4), the distribution of data points on the $\log(P_{\max}) - \log(A)$ diagram appears to be quite regular. Note that for highly absorbing particles (see the left bottom panel in Fig. 4), the 6 points corresponding to different m form almost a straight line. Such quasi-linear behavior holds true for larger x as well, although the slope of the line becomes smaller as x increases. The data points for weakly absorbing particles (right bottom panel in Fig. 4) deviate more significantly from the straight line than those corresponding to highly absorbing particles. This likely is due to the weakly absorbing particles having a greater variance in the real and imaginary

values of the refractive index. However, an increase of size parameter x tends to decrease the deviations from a straight line. We note, when comparing the distributions of the data points in both bottom panels in Fig. 4, one can conclude that they form three trends for Im(m) ≈ 0, Im(m) = 0.02, and Im(m) ≥ 0.05, which are distinct from each another in the log(P_{max}) – log(A) diagram.

Since the non-linear distribution of the data points corresponding to agglomerated debris particles is caused mainly by contribution of small particles with $x < 14$, the study of other types of irregularly shaped particles in this domain of x is of high interest. In the upper row of Fig. 5, we present data from all six different types of irregularly shaped particles, including the agglomerated debris particles. The upper left panel of Fig. 5 shows data for $m = 1.5 + 0.1i$; whereas, the upper right panel shows data for $m = 1.313 + 0i$ and $m = 1.6 + 0.0005i$. Symbols presenting different types of irregular particles appear in different colors (see legend in Fig. 5).

As one can see in the upper row of Fig. 5, all types of irregularly shaped particles produce qualitatively similar distributions of the data points on the diagram log(P_{max}) – log(A); however, some differences are observed. The dispersion of the data points increases with increasing size parameter x. For weakly absorbing particles (upper right panel of Fig. 5), the dispersion of the points respective to different types of irregular particles is significantly greater than that for the points corresponding to agglomerated debris particles with different refractive indices m (c.f. bottom right panel of Fig. 3). In the lower panels of Fig. 5 we calculate the average over the different types. We find that this averaging makes the inverse correlation on the log(P_{max}) – log(A) diagram follow a strong, almost linear trend (right bottom panel of Fig. 5). The trend respective to $m = 1.6 + 0.0005i$ reveals higher slope than that of $m = 1.313 + 0i$. Unlike for the case of weak absorption, averaging over six types of highly absorbing irregular particles produces quite a small impact on the distribution of the data points through the diagram. Indeed, as one can see in the bottom left panel of Fig. 5, it remains qualitatively the same for each single type of irregular particles.

3.3. Impact of the size averaging on diagrams log(P_{max}) – log(A)

Heretofore, we discussed the application of the Umov effect to irregularly shaped particles of fixed size. However, cosmic dust particles as well as particles forming planetary regolith always reveal size polydispersity. For instance, based on *in situ* measurements, the dust particles of comet 1P/Halley follow a power law size distribution r^{-a}, where r is the radius of the equal mass sphere and the power index a is varied from 1.5 to 3.4 over the mass range of dust particles from 10^{-19} to larger than 10^{-12} kg (Mazets et al., 1986). Therefore, for practical

applications, a study of the Umov effect for polydisperse ensembles of irregular particles is essential.

In this sub-section, we present results for the size averaging of agglomerated debris particles having different refractive indices that are listed in Table 1. As can be seen in Table 1, each of the cases has been studied over a wide range of size parameter x, while its minimal value is 2 for all m, the maximal size parameter x is varied from 26 (for $m = 1.5 + 0i$ and $1.6 + 0.0005i$) to 40 ($m = 1.2 + 0i$). When performing size averaging, we set a step of x equal to 2 for entire range of x, i.e. the data corresponding to odd values of x are not taken into account. The power index a is varied from 1.5 to 4 with a step of 0.1. Thus, the range of variations of a covers what was measured in comet 1P/Halley.

Results for the averaging of agglomerated debris particles over size are shown in Fig. 6. All the cases reveal quite regular distributions of the data points on the $\log(P_{\max}) - \log(A)$ diagram, which could be approximated well with a smooth curve. Agglomerated debris particles consisting of optically soft materials with $m = 1.2 + 0i$ and $m = 1.313 + 0i$ show almost linear curves. In these plots, the larger values of the power index a form the upper ranges of the curves; whereas, the smaller values of a are responsible for lower ranges, and the arrowed lines show schematically the dependence on increasing the power index a. Increasing material absorption squeezes and rotates the curved line on the $\log(P_{\max}) - \log(A)$ diagram. This effect can be seen by comparing the curves for $m = 1.6 + 0.0005i$, $1.6 + 0.02i$, and $1.6 + 0.1i$. Increasing $\mathrm{Re}(m)$ stretches and shifts the curves from left to right on the diagram. Note that despite the non-linear behavior, the curves corresponding to weakly absorbing particles (right panel in Fig. 6) hold an inverse correlation between $\log(P_{\max})$ and $\log(A)$, while the highly absorbing particles do not.

3.4. Implications for comets

Using the $\log(P_{\max}) - \log(A)$ diagram, we could try to estimate the geometric albedo of dust particles forming a circumnuclear halo of comets (e.g., Levasseur-Regourd, 1999; Hadamcik and Levasseur-Regourd, 2003), which is the relatively bright, small portion of the inner coma that may surround a cometary nucleus. Typically, the radius of a halo does not exceed a few thousands of kilometers. A distinctive feature of the halo is a strong negative polarization branch observed at small phase angles, the amplitude of which can be up to 6%. Moreover, in numerous polarimetric images of various comets, the halo region reveals the strongest negative polarization within the cometary coma (Hadamcik and Levasseur-Regourd, 2003). As was found in Zubko et al. (2009a), the strong negative polarization clearly indicates a lack of highly absorbing materials in the haloes. For instance, if the real part of refractive index

is Re(m) = 1.5, the upper limit for the imaginary part of refractive index Im(m) is approximately 0.02 (Zubko et al., 2009a).

Interestingly, a circumnuclear halo is visible only during relatively weak jet activity of comets (Hadamcik and Levasseur-Regourd, 2003). We note that low cometary activity correlates with large heliocentric distances. Indeed, such observations imply that the comet has approached closely to the Sun, i.e. with a heliocentric distance of about 1 A.U. or less; however, such approaches significantly increase the activity of a comet that will hide its halo. This problem could be solved using spacecraft-born polarimetry during an encounter with a comet at large heliocentric distance. So far, there are only two successful examples of polarimetric observations performed with using spacecraft. Both have been made within the Optical Probe Experiment (OPE) on board the Giotto space probe. The first one was of comet 1P/Halley at phase angle α = 73° (Levasseur-Regourd et al., 1999); the second one was of comet 26P/Grigg-Skjellerup at α = 90.4° (McBride et al., 1997). Combining the data of ground-based observations obtained by Hadamcik and Levasseur-Regourd (2003) with those received with the OPE, one can obtain the maximum of positive polarization P_{max} of haloes. According to Zubko et al. (2009a), this could be approximately 12%. Simultaneously, as was shown in that paper, there is a strong correlation between a deep negative polarization branch at small phase angles and a low positive polarization at intermediate phase angles of particles comparable with wavelength. In particular, P_{max} = 12% is consistent with P_{min} = –6%. Nevertheless, while attributing P_{max} = 12% to circumnuclear haloes, we stress that more polarimetric observations of haloes are needed to assure the derived value of amplitude of positive polarization.

Based on the amplitude of the positive polarization branch of haloes, we could derive an approximate geometric albedo A of the dust particles forming a cometary halo. Fig. 6 is the most suitable for this purpose, since it presents results averaged over size with a power law distribution. The same size distribution has been found from *in situ* measurements of dust particles in the coma of comet 1P/Halley (e.g., Mazets et al., 1986). The horizontal dashed line in both panels of Fig. 6 shows the positive polarization maxima corresponding to the haloes. As one can see from the left panel in Fig. 6, all the modeling data corresponding to highly absorbing particles are located distantly from this dashed line: this is consistent with the previous conclusion of the absence of highly absorbing particles in circumnuclear haloes (Zubko et al., 2009a). Simultaneously, some curves in the right panel of Fig. 6 do cross the dash line, namely modeling data for m = 1.5 + 0i, 1.6 + 0.0005i, and 1.6 + 0.02i. Therefore, the data suggest agglomerated debris particles having a real refractive index Re(m) = 1.5–1.6 and an imaginary refractive index less than approximately Im(m) = 0.02. It is worth noting that the refractive

indices m = 1.5 + 0i and 1.6 + 0.0005i correspond well with Mg-rich silicates in visible wavelengths (Dorschner *et al*., 1995) and refractive indices having greater absorption, toward m = 1.6 + 0.02i could be associated with either Mg-rich silicates with a very small admixture of iron (Dorschner et al., 1995) or organic material kerogen type II at wavelengths exceeding 0.5 μm (Khare et al., 1990). Note that the first two cases belong to the so-called ROCK component of comets; kerogen type II could belong to the so-called CHON component of comets. According to *in situ* measurements of comet 1P/Halley, ROCK and CHON are the most abundant components of comets (e.g., Jessberger, 1999). From Fig. 6, one can derive $A \approx 0.18$ for the case of m = 1.5 + 0i, $A \approx 0.2$ for the case of m = 1.6 + 0.0005i, and $A \approx 0.11$ for m = 1.6 + 0.2i. These values are visibly higher than that of the entire coma $A \approx 0.05$ (Hanner, 2003). Interestingly, agglomerated debris particles fit the polarization maximum of haloes at values of the power-law size-distribution index a = 2 (m = 1.5 + 0i), a = 2.5 (m = 1.6 + 0.0005i), and a = 1.9 (m = 1.6 + 0.02i).

Finally, we note that agglomerated debris particles consisting of optically soft material fail to fit the maximum of linear polarization observed in circumnuclear haloes. As we noted in section 2, optically soft materials often are used to approximate light-scattering properties of fluffy particles using effective medium theories, e.g., weakly absorbing silicates. We conclude that dust particles significantly fluffier than agglomerated debris particles do not appear in considerable quantities in haloes.

3.5. The log(h) – log(A) diagram

An obvious difficulty accompanying the application of the Umov effect for the interpretation of ground-based polarimetric observations of asteroids and planetary satellites is caused by the range of small phase angles that can be achieved for distant objects, as the maximum positive polarization is typically observed at large α. For instance, the linear polarization of cometary circumnuclear haloes have maxima near α = 60º (Zubko et al., 2009a). The location of the positive polarization maximum of atmosphereless celestial bodies also occurs over a wide range of large phase angles. For the Moon, it occurs at α ≈ 95–110º (e.g., Shkuratov and Opanasenko, 1992). For the heliocentric distance of Mars (1.5 A.U.), the maximal phase angle that can be achieved with ground-based observations is approximately 48º, which does not allow for its positive polarization maximum to be measured from Earth. Such a limitation inspired the search for analogs of the Umov effect at smaller α (e.g., Geake and Dollfus, 1986; Shkuratov et al., 1992; Shkuratov and Opanasenko, 1992; Wolff, 1980). For asteroids and

planetary satellites, instead of using the Umov effect, reliable estimates of geometric albedo can be carried out using the inverse correlation $\log(h) - \log(A)$, where h is the slope of the polarization curve at the inversion angle (e.g., Cellino et al., 1999; 2005; Geake and Dollfus, 1986; Lupishko and Mohamed, 1996; Shkuratov, 1980; Shkuratov et al., 1992; Wolff, 1980; Zellner et al., 1977a,b). This inverse correlation could be considered as an analog of the Umov effect. Note that in cometary applications, the slope of polarization curve h is also considered as a valuable parameter (e.g., Chernova et al., 1993; Boehnhardt et al., 2008).

We study a possible correlation $\log(h) - \log(A)$ for the average over six types of irregular particles previously considered in Section 3.2. For materials with $\mathrm{Im}(m) \leq 0.02$, such an averaging reveals a linear inverse correlation $\log(P_{\max}) - \log(A)$ that is qualitatively the same as the manifestation of the Umov effect for regoliths. Figure 7 presents the $\log(h) - \log(A)$ diagram for the average over six types of irregular particles. The left and right panels correspond to highly and weakly absorbing particles, respectively.

Note that the slope of the polarization curve h is formally defined at the phase angle of polarization sign inversion, i.e., when the polarization is 0. However, the average profile of linear polarization of irregularly shaped particles with $x = 2$ do not have a negative polarization branch; the same holds true for $x = 4$ at $m = 1.5 + 0.1i$ and $m = 1.313 + 0i$. Therefore, we exclude these cases from our study of correlation between $\log(h)$ and $\log(P_{\max})$.

We do not find a reliable correlation between $\log(h)$ and $\log(A)$. This suggests that for single particles comparable with wavelength, the positive and negative polarization branches have different origins, and thus the parameter h does not have a simple physical meaning. On the other hand, the inverse correlation held for regoliths with high and moderate brightness (Hapke, 1993; Shkuratov, 1980; Wolff, 1980; Zellner et al., 1977a,b), and one can conclude that in this case h does have a simple physical meaning.

4. Conclusion

In this paper we have studied an extension of the Umov effect for the case of single irregularly shaped particles comparable with wavelength. The principal results of this research can be summarized as follows:

1. For single particles comparable to the wavelength the Umov effect is defined in terms of geometric albedo rather than to single-scattering albedo.

2. The Umov effect holds for weakly absorbing irregular particles comparable with wavelength (Im(m) ≤ 0.02) almost through the entire range size parameters x studied in this manuscript.

3. The Umov effect holds for highly absorbing particles (Im(m) > 0.02) only when their size parameters are large, x > 14.

4. For weakly absorbing particles, a non-linear inverse correlation between log(P_{max}) and log(A) is the result of particles having small values of size parameter x = 2 – 14. However, averaging over many different types of irregularly shaped particles makes the correlation significantly more linear. For highly absorbing particles such averaging has no significant effect on the distribution of data points throughout the log(P_{max}) – log(A) diagram.

5. The size averaging of irregularly shaped particles does not change qualitatively the distribution of the data points on the log(P_{max}) – log(A) diagram, although it reduces the deviation of the data points from the general trend. In other words, if the inverse correlation is non-linear for particles of a fixed size, the size averaging does not linearize it.

6. For single irregular particles comparable with wavelength there is no reliable correlation between the parameters h and A. Therefore, unlike asteroids, the slope of the polarization curve h observed for comets has no simple connection with dust-particle properties.

7. Using the log(P_{max}) – log(A) diagram computed for size-averaged agglomerated debris particles, we estimate the geometric albedo A of dust particles forming cometary circumnuclear haloes as $A \approx 0.1 – 0.2$. This value is a few times larger than A averaged over the entire coma. Simultaneously, the power law distribution index a is found to be $a \approx 1.9 – 2.5$.

Acknowledgment

We are grateful to Prof. A.Ch. Levasseur-Regourd for her comments on this paper. Research by EZ and KM was partially supported by the Academy of Finland (contract 1127461). TY acknowledges support by the Grant-in-Aid for Scientific Research from JSPS (21244011).

References

Asano, S., Sato, M., 1980. Light scattering by randomly oriented spheroidal particles. Appl. Opt. 19, 962–974.

Avramchuk, V.V., 1964. Polychromatic polarimetry of some lunar regions. In: Koval', I.K. (Ed.), Physics of the Moon and the Planets. Naukova Dumka, Kiev, Ukraine, pp. 3–15. [In Russian]. Trans. From Russian: Israel Program for Scientific Trans., Jerusalem, Israel, pp. 1–10 (IPST Cat, No.1548).

Boehnhardt, H., Tozzi, G.P., Bagnulo, S., Muinonen, K., Nathues A., Kolokolova, L., 2008. Photometry and polarimetry of the nucleus of comet 2P/Encke. Astron. Astrophys. 489, 1337–1343.

Bohren, C.F., Huffman, D.R., 1983. Absorption and Scattering of Light by Small Particles. Wiley, New York.

Cellino, A., Gil Hutton, R., Tedesco, E. F., di Martino, M., Brunini, A., 1999. Polarimetric observations of small asteroids: preliminary results. Icarus. 138, 129–140.

Cellino, A., Yoshida, F., Anderlucci E., Bendjoya, P., di Martino, M., Ishiguro, M., Nakamura, A. M., Saito, J., 2005. A polarimetric study of asteroid 25143 Itokawa. Icarus. 179, 297–303.

Clarke, D., 1965. Studies in astronomical polarimetry III. Mon. Not. Roy. Astron. Soc. 130, 83–94.

Chernova, G.P., Kiselev, N.N., Jockers, K., 1993. Polarimetric characteristics of dust particles as observed in 13 comets – Comparisons with asteroids. Icarus 103, 144–158.

Dollfus A., Bowell E., 1971. Polarimetric properties of the lunar surface and interpretation. Part I. Telescope observation. Astron. Astrophys. 10. 29-53.

Dollfus, A., Bowell, E., Titulaer, C., 1971. Polarimetric properties of the lunar surface and its interpretation. Part II. Terrestrial samples in orange light. Astron. Astrophys. 10, 450–466.

Dollfus, A., Titulaer, C., 1971. Polarimetric properties of the lunar surface and its interpretation. Part III. Volcanic samples in several wavelengths. Astron. Astrophys. 12, 199–209.

Dollfus, A., 1998. Lunar surface imaging polarimetry. I. Roughness and grain size. Icarus 135, 69–103.

Dorschner, J., Begemann, B., Henning, T., Jaeger, C., Mutschke, H., 1995. Steps toward interstellar silicate mineralogy. II. Study of Mg-Fe-silicate glasses of variable composition. Astron. Astrophys. 300, 503–520.

Draine, B., 1988. The discrete-dipole approximation and its application to the interstellar graphite grains. Astrophys. J. 333, 848–872.

Draine, B.T., Flatau, P.J., 1994. The discrete dipole approximation for scattering calculations. J. Opt. Soc. Am. A 11, 1491–1499.

Geake, J.E., Dollfus, A., 1986. Planetary surface texture and albedo from parameter plots of optical polarization data. Mon. Not. Roy. Astron. Soc. 218, 75–91.

Goodman, J.J., Draine, B.T., Flatau, P.J., 1991. Application of fast-Fourier-transform techniques to the discrete-dipole approximation. Opt. Lett. 16, 1198–1200.

Grynko, Ye., Jockers, K., Schwenn, R., 2004. The phase curve of cometary dust: Observations of comet 96P/Machholz 1 at large phase angle with the SOHO LASCO C3 coronagraph. Astron. Astrophys. 427, 755–761.

Hadamcik, E., Levasseur-Regourd, A.C., 2003. Imaging polarimetry of cometary dust: different comets and phase angles. J. Quant. Spectrosc. Radiat. Transfer 79-80, 661–678.

Hadamcik, E., Renard, J., Worms, J., Levasseur-Regourd, A.-C., Masson, M., 2002. Polarization of Light Scattered by Fluffy Particles (PROGRA2 Experiment). Icarus 155, 497–508.

Hanner, M.S., Giese, R.H., Weiss, K., Zerull, R., 1981. On the definition of albedo and application to irregular particles. Astron. Astrophys. 104, 42–46.

Hanner, M.S., 2003. The scattering properties of cometary dust. J. Quant. Spectrosc. Radiat. Transfer 79-80, 695–705.

Harris, A.W., Mueller, M., Delbó, M., Bus, S.J., 2007. Physical characterization of the potentially hazardous high-albedo Asteroid (33342) 1998 WT_{24} from thermal-infrared observations. Icarus 188, 414–424.

Hapke, B., 1993. Theory of Reflectance and Emittance Spectroscopy. Cambridge Univ. Press, Cambridge.

Jenniskens, P., 1993. Optical constants of organic refractory residue. Astron. Astrophys. 274, 653–661.

Jessberger, E.K., 1999. Rocky cometary particulates: their elemental isotopic and mineralogical ingredients. Space Science Rev. 90, 91–97.

Karttunen, H., Kröger, P., Oja, H., Poutanen, M., Donner, K.J., 1996. Fundamental Astronomy. Springer-Verlag, Berlin–Heidelberg–New York.

Kornienko, Y.V., Shkuratov, Y.G., Bychinskii, V.I., Stankevich, D.G., 1982. Correlation between albedo and polarization characteristics of the Moon – application of digital image processing. Soviet astronomy 26, 345–348.

Khare, B.N., Thompson, W.R., Sagan, C., Arakawa, E.T., Meisse, C., Gilmour, I., 1990. Optical constants of kerogen from 0.15 to 40 μm: comparison with meteoritic organics. Proc. Lunar Planet. Sci. Conf. 21, 627–628.

Khare, B.N., Thompson, W.R., Cheng, L., Chyba, C., Sagan, C., Arakawa, E.T., Meisse, C., Tuminello, P.S., 1993. Production and optical constants of ice tholin from charged particle irradiation of (1:6) C_2H_6/H_2O at 77K. Icarus 103, 290–300.

Kimura, H., 2001. Light-scattering properties of fractal aggregates: numerical calculations by a superposition technique and the discrete-dipole approximation. J. Quant. Spectrosc. Radiat. Transfer 70, 581–594.

Kimura, H., Chigai, T., Yamamoto, T., 2008. Mid-infrared spectra of cometary dust: the evasion of its silicate mineralogy. Astron. Astrophys. 482, 305–307.

Lasue, J., Levasseur-Regourd, A.C., Hadamcik, E., Alcouffe, G., 2009. Cometary dust properties retrieved from polarization observations: Application to C/1995 O1 Hale Bopp and 1P/Halley. Icarus 199, 129–144.

Levasseur-Regourd, A.C., Cabane, M., Worms, J.C., Haudebourg, V., 1997. Physical properties of dust in the solar system: Relevance of a computational approach and of measurements under microgravity conditions. Adv. Space Res. 20, 1585–1594.

Levasseur-Regourd, A.C., 1999. Polarization of light scattered by cometary dust particles: observations and tentative interpretations. Space Sci. Rev. 90, 163–168.

Levasseur-Regourd, A.C., McBride, N., Hadamcik, E., Fulle, M., 1999. Similarities between in situ measurements of local dust light scattering and dust flux impact data within the coma of 1P/Halley. Astron. Astrophys. 348, 636–641.

Lupishko, D., Mohamed, R., 1996. A new calibration of the polarimetric albedo scale of asteroids. Icarus 119, 209–213.

Lyot, B., 1929. Recherches sur la polarisation de la lumiere des planetes et de queldues substances terrestres. Ann. Obs. Meudon 8, 1–161.

Mazets, E.P., Aptekar, R.L., Golenetskii, S.V., Guryan, Yu.A., Dyachkov, A.V., Ilyinskii, V.N., Panov, V.N., Petrov, G.G., Savvin, A.V., Sagdeev, R.Z., Sokolov, I.A., Khavenson, N.G.,

Shapiro, V.D., Shevchenko, V.I., 1986. Comet Halley dust environment from SP-2 detector measurements. Nature 321, 276–278.

McBride, N., Green, S.F., Levasseur-Regourd, A.C., Goidet-Devel, B., Renard, J.B., 1997. The inner dust coma of Comet 26P/Grigg-Skjellerup: multiple jets and nucleus fragments? Mon. Not. Roy. Astron. Soc. 289, 535–553.

Mishchenko, M.I., Liu, L., Hovenier, J.W., 2007. Effects of absorption on multiple scattering by random particulate media: exact results. Opt. express 15, 13182–13187.

Muinonen, K., Nousiainen, T., Fast, P., Lumme, K., Peltoniemi, J.I., 1996. Light scattering by Gaussian random particles: ray optics approximation. J. Quant. Spectrosc. Radiat. Transfer 55, 577–601.

Novikov, V.V., Shkuratov, Y.G., Popov, A.P., Goryachev, M.V., 1982. Correlation between albedo and polarization properties of the Moon (heterogeneity of the relative porosity of the surface of the western part of the visible hemisphere). Soviet Astronomy 26, 79–83.

Opanasenko, N.V., Shkuratov, Yu.G., 1994. Results of simultaneous polarimetry and photometry of the Moon. Solar System Res. 28, 233–254.

Ovcharenko, A.A., Bondarenko, S.Yu., Zubko, E.S., Shkuratov, Yu.G., Videen, G., Nelson, R., 2006. Particle size effect on the opposition spike and negative polarization. J. Quant. Spectrosc. Radiat. Transfer 101, 394–403.

Pellicori, S.F., 1969. Polarization – albedo relationship for selected lunar regions. Commun. Lunar Planet. Lab. 8, 73–74.

Penttilä, A., Lumme, K., Worms, J.C., Hadamcik, E., Renard, J.B., Levasseur-Regourd, A.C., 2003. Theoretical analysis of the particle properties and polarization measurements made in microgravity. J. Quant. Spectrosc. Radiat. Transfer 79–80, 1043–1049.

Penttilä, A., Zubko, E., Lumme, K., Muinonen, K., Yurkin, M.A., Draine, B., Rahola, J., Hoekstra, A.G., Shkuratov, Yu., 2007. Comparison between discrete dipole implementations and exact techniques. J. Quant. Spectrosc. Radiat. Transf. 106, 417–436.

Pollack, J. B., Hollenbach, D., Beckwith, S., Simonelli, D.P., Roush, T., Fong, W., 1994. Composition and radiative properties of grains in molecular clouds and accretion disks. Astrophys. J. 421, 615–639.

Provostaye, F., Desains, P., 1852. Mémoire sur la diffusion de la chaleur. Annales de Chimie et de Physique 34, 192–225.

Purcell, E.M., Pennypacker, C.R., 1973. Scattering and absorption of light by nonspherical dielectric grains. Astrophys. J. 186, 705–714.

Shkuratov, Yu.G., 1980. Albedos of asteroids. Soviet Astronomy 24, 760–761.

Shkuratov, Yu.G., 1981. Connection between the albedo and polarization properties of the Moon. Fresnel component of reflected light. Soviet Astronomy 25, 490–494.

Shkuratov, Yu.G., Opanasenko, N.V., 1992. Polarimetric and photometric properties of the Moon: Telescope observation and laboratory simulation. 2. The positive polarization. Icarus 99, 468–484.

Shkuratov, Yu.G., Opanasenko, N.V., Kreslavsky, M.A., 1992. Polarimetric and photometric properties of the Moon: Telescope observation and laboratory simulation. 1. The negative polarization. Icarus 95, 283–299.

Shkuratov, Yu.G., Muinonen, K., Bowell, E., Lumme, K., Peltoniemi, J., Kreslavsky, M.A., Stankevich, D.G., Tishkovetz, V.P., Opanasenko, N.V., Melkumova, L.Ya., 1994. A critical review of theoretical models for the negative polarization of light scattered by atmosphereless solar system bodies. The Earth, Moon, and Planets 65, 201–246.

Shkuratov, Yu.G., Opanasenko, N.V., 1994. Is there Umov effect for the Moon in polarization minimum? Proc. Lunar Planet. Sci. Conf. 25. 1271–1272.

Shkuratov, Yu., Ovcharenko, A., Zubko, E., Miloslavskaya, O., Muinonen, K., Piironen, J., Nelson, R., Smythe, W., Rosenbush, V., Helfenstein, P., 2002. The opposition effect and negative polarization of structural analogs for planetary regoliths. Icarus 159, 396–416.

Shkuratov, Yu.G., Grynko, Ye.S., 2005. Scattering by semitransparent particles of different shapes and media consisting of these particles in geometric optics approximation: consequences for photometry and spectroscopy of the planetary regoliths. Icarus 173, 16–28.

Shkuratov, Yu., Opanasenko, N., Zubko, E., Grynko, Ye., Korokhin, V., Pieters, C., Videen, G., Mall, U., Opanasenko, A., 2007. Multispectral polarimetry as a tool to investigate texture and chemistry of lunar regolith particles. Icarus 187, 406–416.

Toporets, A.S, 1950. Umov effect. J. Experim. Theoret. Phys. 20, 390–394. [In Russian]

Tyynelä, J., Zubko, E., Muinonen, K., Videen, G., 2010. Interpretation of single-particle negative polarization at intermediate scattering angles, Appl. Opt. 49, 5284–5296.

Umov, N.A., 1905. Chromatische depolarisation durch lichtzerstreung. Phis. Zeits. 6, 674–676.

Warren, S.G., 1984. Optical constants of ice from the ultraviolet to the microwave. Appl. Opt. 23, 1206–1225.

Woessner, P., Hapke, B., 1987. Polarization of light scattered by clover. Remote Sensing of Environ. 21, 243–261.

Wolff, M., 1980. Theory and application of the polarization-albedo rules. Icarus 44, 780–792.

Yurkin, M.A., Hoekstra, A.G., 2007. The discrete dipole approximation: An overview and recent developments. J. Quant. Spectrosc. Radiat. Transfer 106, 558–589.

Zellner, B., Gehrels, T., Gradie, J., 1974. Minor planets and related objects. XVI. Polarimetric diameters. Astron. J. 79, 1100–1110.

Zellner, B., Leak M., Lebertre, T. Duseaux, M., Dollfus, A., 1977a. The asteroid albedo scale. I. Laboratory polarimetry of meteorites. Proc. Lunar Planet. Sci. Conf. 8. 1091–1110.

Zellner, B., Lebertre, T. Day, K., 1977b. The asteroid albedo scale. II. Laboratory poalarimetry of dark carbon-bearing silicates. Proc. Lunar Planet. Sci. Conf. 8. 1111–1117.

Zubko, E., Shkuratov, Yu., Kiselev, N., Videen, G., 2006. DDA simulations of light scattering by small irregular particles with various structure. J. Quant. Spectrosc. Radiat. Transfer 101, 416–434.

Zubko, E., Muinonen, K., Shkuratov, Yu., Videen, G., Nousiainen, T., 2007. Scattering of light by roughened Gaussian random particles. J. Quant. Spectrosc. Radiat. Transfer 106, 604–615.

Zubko, E., Shkuratov, Yu., Mishchenko, M., Videen, G., 2008. Light scattering in a finite multi-particle system. J. Quant. Spectrosc. Radiat. Transfer 109, 2195–2206.

Zubko, E., Kimura, H., Shkuratov, Yu., Muinonen, K., Yamamoto, T., Okamoto, H., Videen, G., 2009a. Effect of absorption on light scattering by agglomerated debris particles. J. Quant. Spectrosc. Radiat. Transfer 110, 1741–1749.

Zubko, E., Furusho, R., Yamamoto, T., Videen, G., Muinonen, K., 2009b. Interpretation of photo-polarimetric observations of comet 17P/Holmes during outburst in 2007. Bull. Am. Astron. Soc. 41, 1035.

Zubko, E., Petrov, D., Grynko, Y., Shkuratov, Yu., Okamoto, H., Muinonen, K., Nousiainen, T., Kimura, H., Yamamoto, T., Videen, G., 2010. Validity criteria of the discrete dipole approximation. Appl. Opt. 49, 1267–1279.

Captions for Figures and Table

Fig. 1. Log(P_{max}) vs. log(A) diagram for 22 sites on the Moon (adapted from Shkuratov et al., 1992).

Fig. 2. Sample images of the six types of irregularly shaped particles used in this study.

Fig. 3. Log(P_{max}) vs. log(ω) diagram (top) and vs. log(A) (bottom) for agglomerated debris particles. The left and right panels present highly (Im(m) > 0.02) and weakly (Im(m) ≤ 0.02) absorbing particles, respectively. Everywhere, red symbols correspond to x = 2, orange symbols to x = 10, green symbols to x = 20, and blue symbols to x = 30. Arrowed lines in the bottom panels show schematically the dependence of data point location on size parameter x at given refractive index m.

Fig. 4. Log(P_{max}) vs. log(A) diagrams for agglomerated debris particles. The left panels present highly absorbing particles (Im(m) > 0.02), and the right panels corresponds to weakly absorbing particles (Im(m) ≤ 0.02). The upper and bottom rows show the data at $x \geq 14$ and x = 14, respectively. Green and blue symbols in the upper row represent the cases of x = 20 and 30, respectively.

Fig. 5. Log(P_{max}) vs. log(A) diagrams for six different types of irregularly shaped particles with size parameter x varying from 2 to 14 with step of 2. The left panels show results for highly absorbing particles (Im(m) > 0.02), and the right panels show results for weakly absorbing particles (Im(m) ≤ 0.02). The upper panels correspond to all cases separately, and the bottom panels show the data averaged over the six types of irregular particles. Numbers in the bottom panels present values of size parameter x.

Fig. 6. Log(P_{max}) vs. log(A) diagrams for agglomerated debris particles averaged over size with power law size distribution r^{-a}. The left panels show results for highly absorbing particles (Im(m) > 0.02), and the right panels show results for weakly absorbing particles (Im(m) ≤ 0.02). Arrowed lines show schematically the dependence of data point location on the power index a at given refractive index m. The power index a is varied from 1.5 to 4.

Fig. 7. Log(h) vs. log(A) diagrams for the average over six different types of irregularly shaped particles. The left panels show results for highly absorbing particles (Im(m) > 0.02), and the right panels show results for weakly absorbing particles (Im(m) ≤ 0.02). Each point corresponds to a fixed value of size parameter x. The range of x is shown by numbers at the ends of each curve.

Table 1. List of sets of refractive index m and size parameter x of agglomerated debris particles that have been considered in the current study. Symbol "x" indicates a set of parameters investigated; whereas, an empty cell corresponds to non-investigated case.

m / x	$1.2+0i$	$1.313+0i$	$1.313+0.1i$	$1.4+0i$	$1.5+0i$	$1.5+0.02i$	$1.5+0.1i$	$1.6+0.0005i$	$1.6+0.01i$	$1.6+0.02i$	$1.6+0.05i$	$1.6+0.1i$	$1.7+0i$	$1.7+0.1i$	$1.758+0.0844i$
2	x	x	x	x	x	x	x	x	x	x	x	x	x	x	x
3	x	x	x		x	x	x	x		x		x		x	
4	x	x	x	x	x	x	x	x	x	x	x	x	x	x	x
5	x	x	x		x	x	x	x		x		x		x	
6	x	x	x	x	x	x	x	x	x	x	x	x	x	x	x
7	x	x	x		x	x	x	x		x		x		x	
8	x	x	x	x	x	x	x	x	x	x	x	x	x	x	x
9	x	x	x		x	x	x	x		x				x	
10	x	x	x	x	x	x	x	x	x	x	x	x	x	x	x
11	x	x	x		x	x	x	x		x		x		x	
12	x	x	x	x	x	x	x	x	x	x	x	x	x	x	x
13	x	x	x		x	x	x	x		x		x		x	
14	x	x	x	x	x	x	x	x	x	x	x	x	x	x	x
15	x	x	x			x	x					x		x	
16	x	x	x		x	x	x	x		x		x		x	
17	x	x	x												
18	x	x	x		x	x	x	x		x		x		x	
19	x														
20	x	x	x		x	x	x	x		x		x	x	x	
22	x	x	x		x	x	x	x		x		x		x	
24	x	x	x		x	x	x	x		x		x		x	
26	x	x	x		x	x	x	x		x		x		x	
28	x	x	x			x	x			x		x		x	
30	x	x	x			x	x					x		x	
32	x	x	x				x					x		x	
34	x	x	x												
36	x	x	x												
38	x														
40	x														

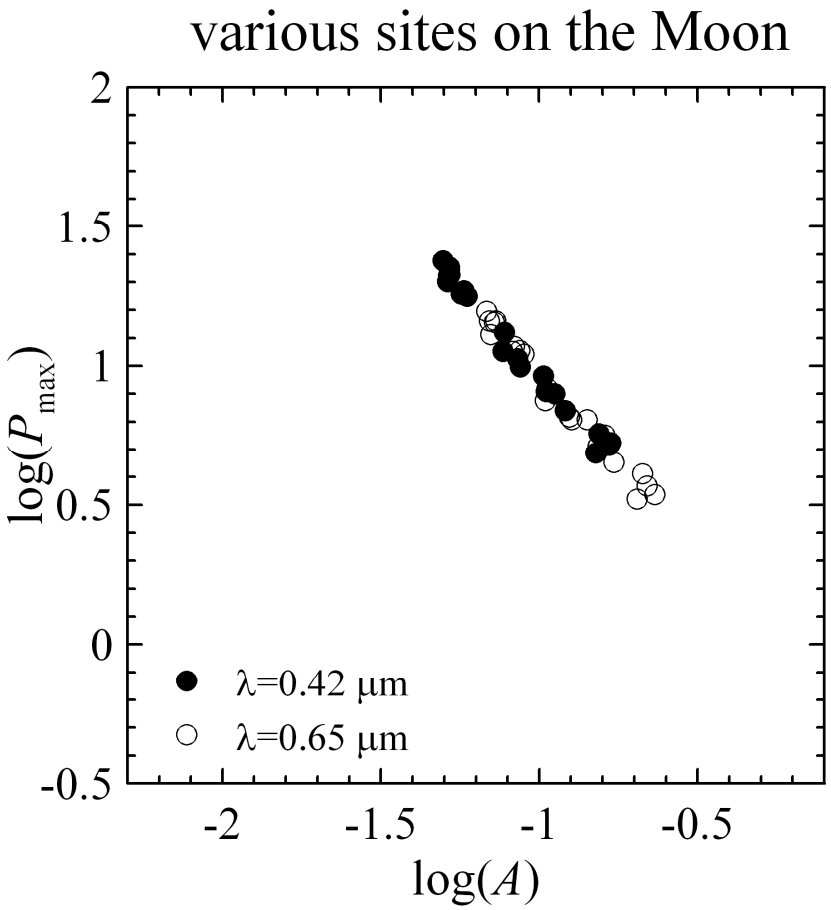
various sites on the Moon
2
1.5
1
0.5
0
-0.5
log(P_max)
-2
-1.5
-1
-0.5
log(A)
λ=0.42 μm
λ=0.65 μm

Fig. 1.

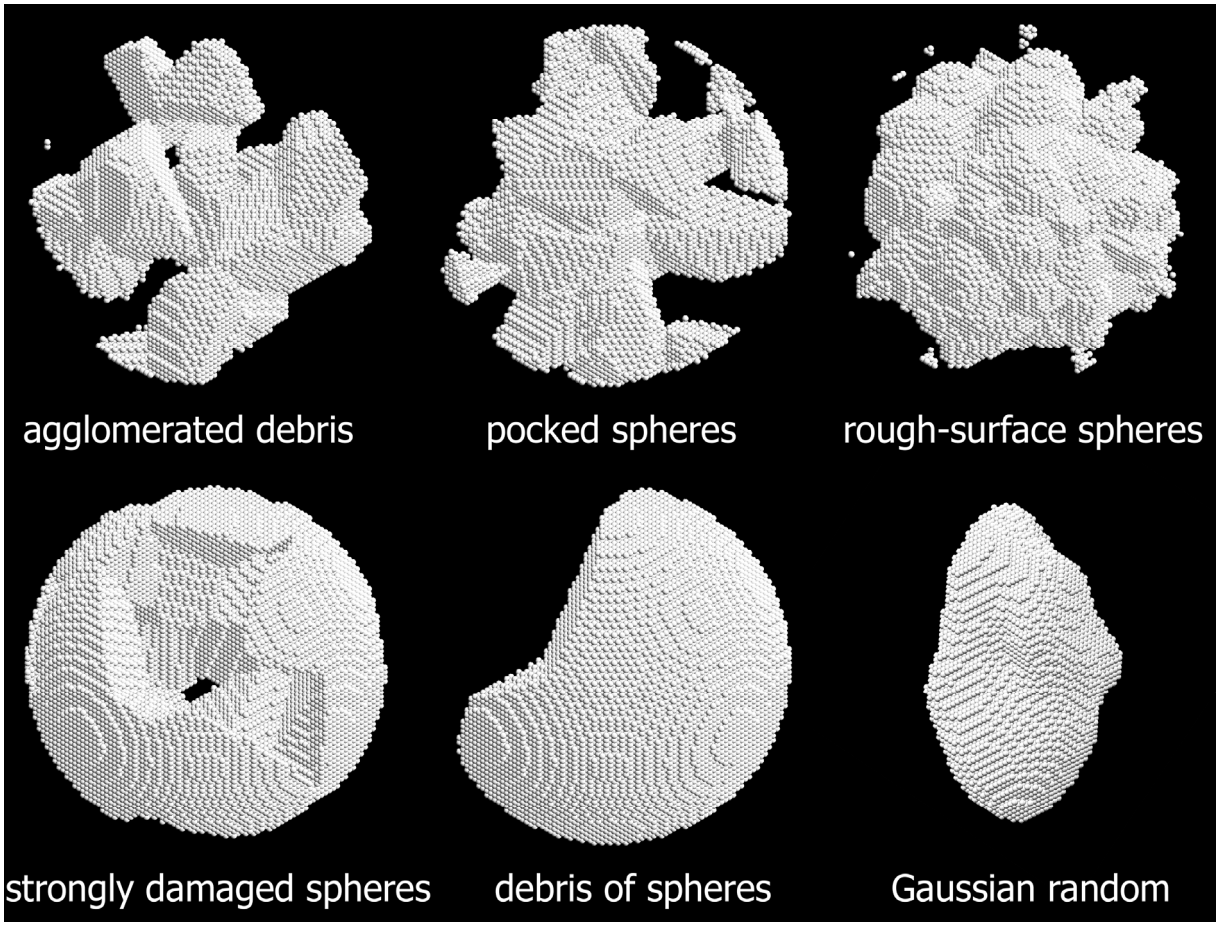
agglomerated debris
pocked spheres
rough-surface spheres
strongly damaged spheres
debris of spheres
Gaussian random

Fig. 2.

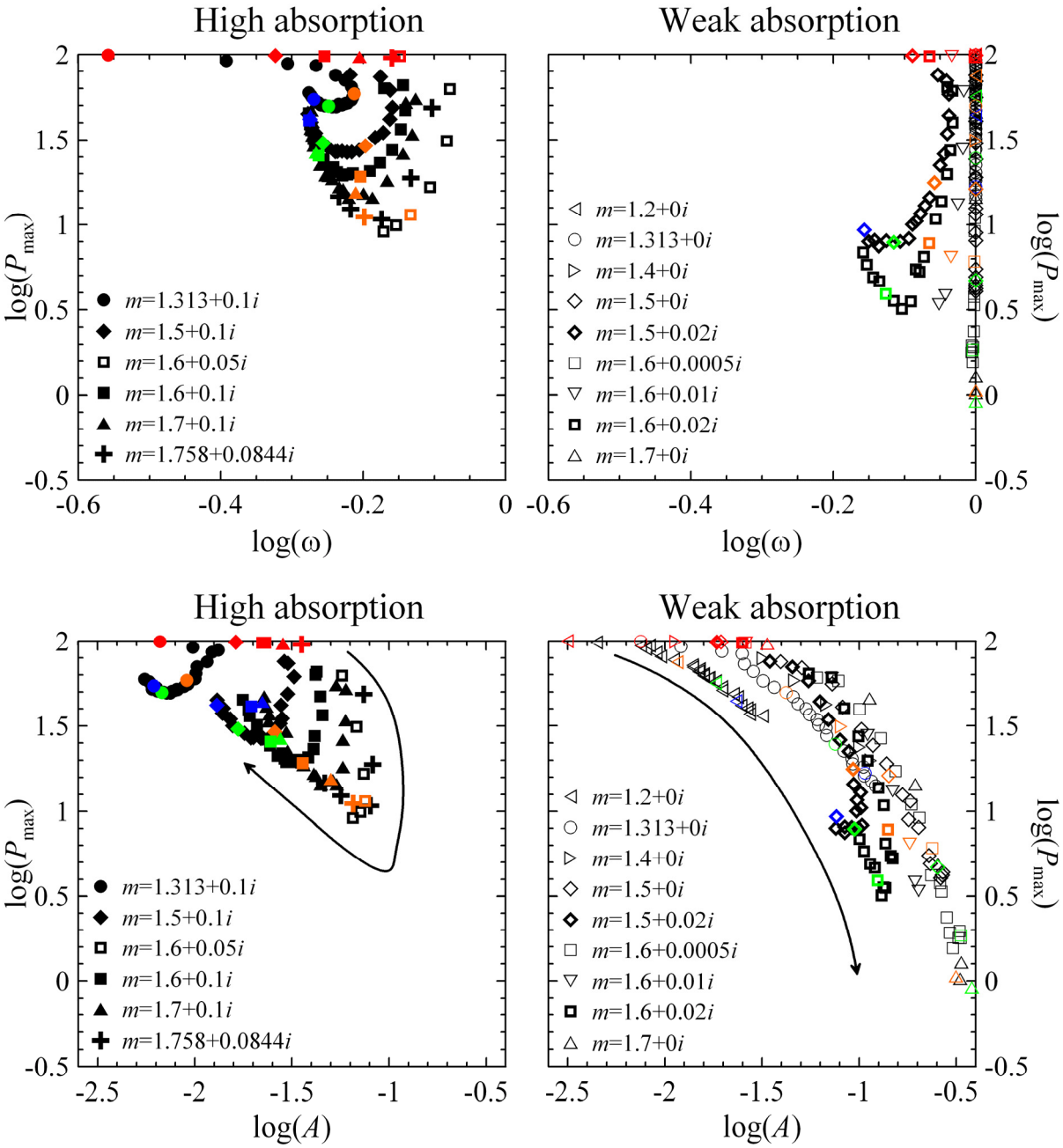
High absorption
Weak absorption
log(P_{max})
log(ω)
log(A)
m=1.313+0.1i
m=1.5+0.1i
m=1.6+0.05i
m=1.6+0.1i
m=1.7+0.1i
m=1.758+0.0844i
m=1.2+0i
m=1.313+0i
m=1.4+0i
m=1.5+0i
m=1.5+0.02i
m=1.6+0.0005i
m=1.6+0.01i
m=1.6+0.02i
m=1.7+0i

Fig. 3.

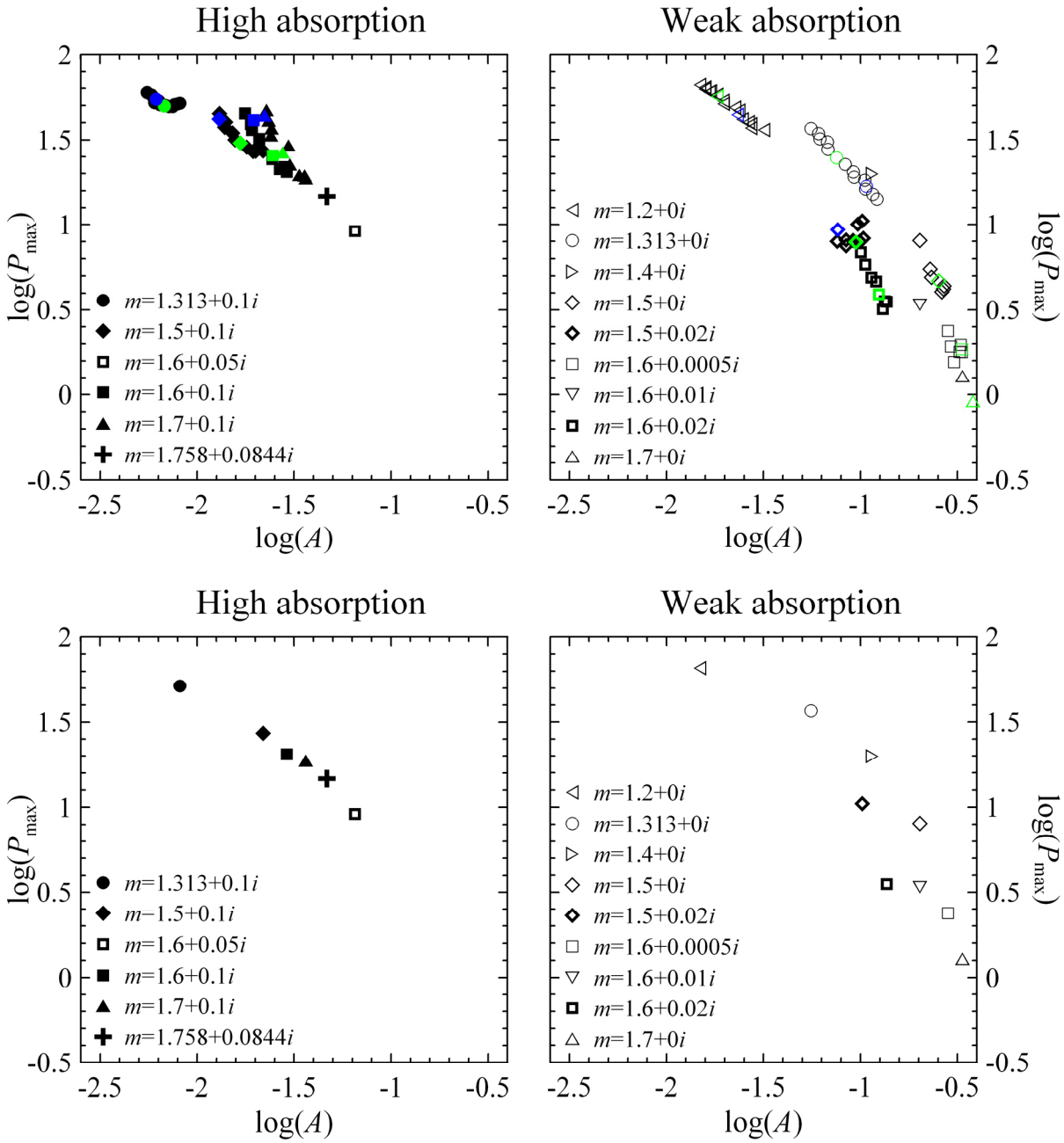
High absorption
Weak absorption
High absorption
Weak absorption
log(P_max)
log(A)
m=1.313+0.1i
m=1.5+0.1i
m=1.6+0.05i
m=1.6+0.1i
m=1.7+0.1i
m=1.758+0.0844i
m=1.2+0i
m=1.313+0i
m=1.4+0i
m=1.5+0i
m=1.5+0.02i
m=1.6+0.0005i
m=1.6+0.01i
m=1.6+0.02i
m=1.7+0i

Fig. 4.

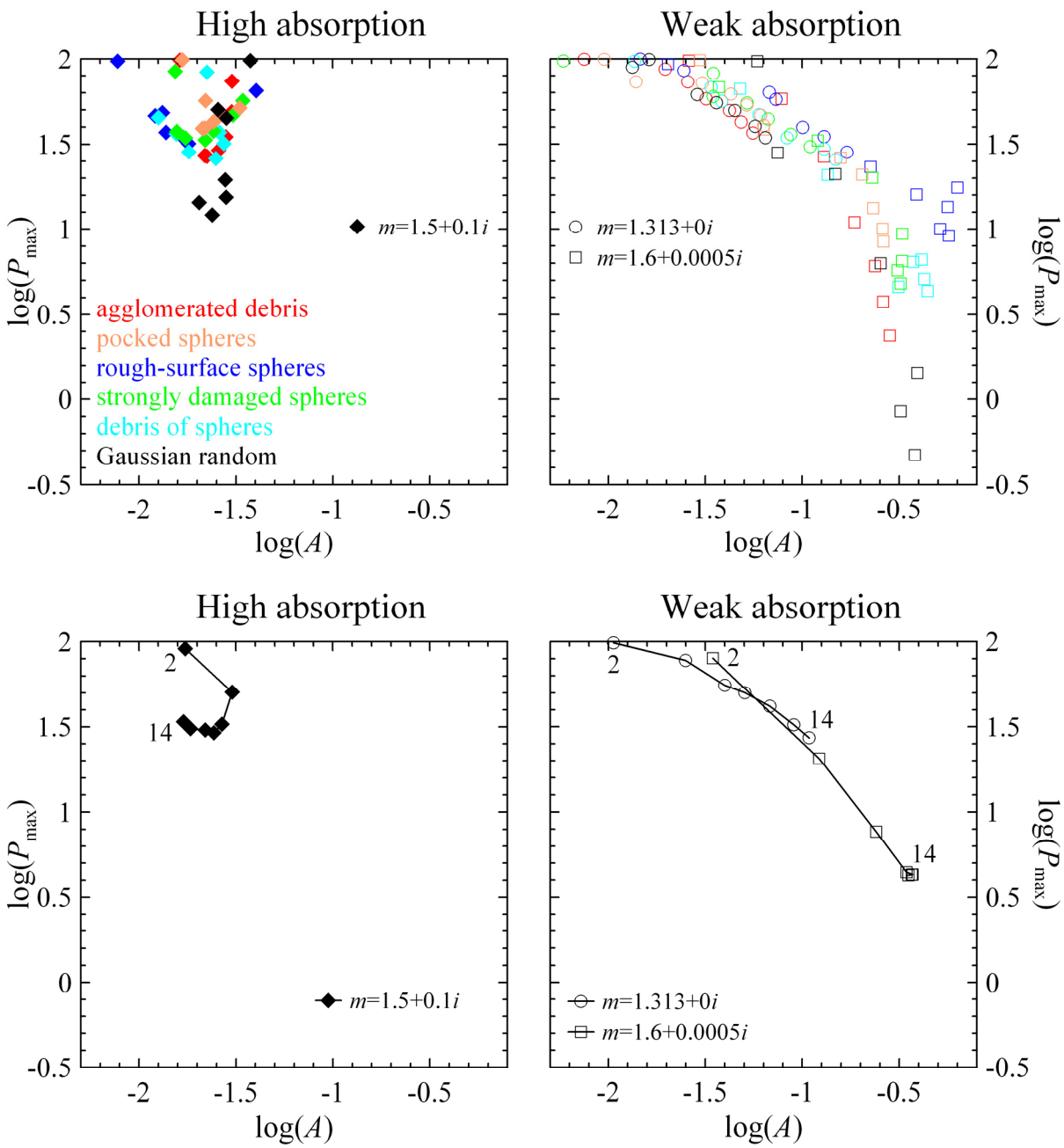
High absorption
Weak absorption
log(P_max)
log(A)
m=1.5+0.1i
m=1.313+0i
m=1.6+0.0005i
agglomerated debris
pocked spheres
rough-surface spheres
strongly damaged spheres
debris of spheres
Gaussian random
2
14

Fig. 5.

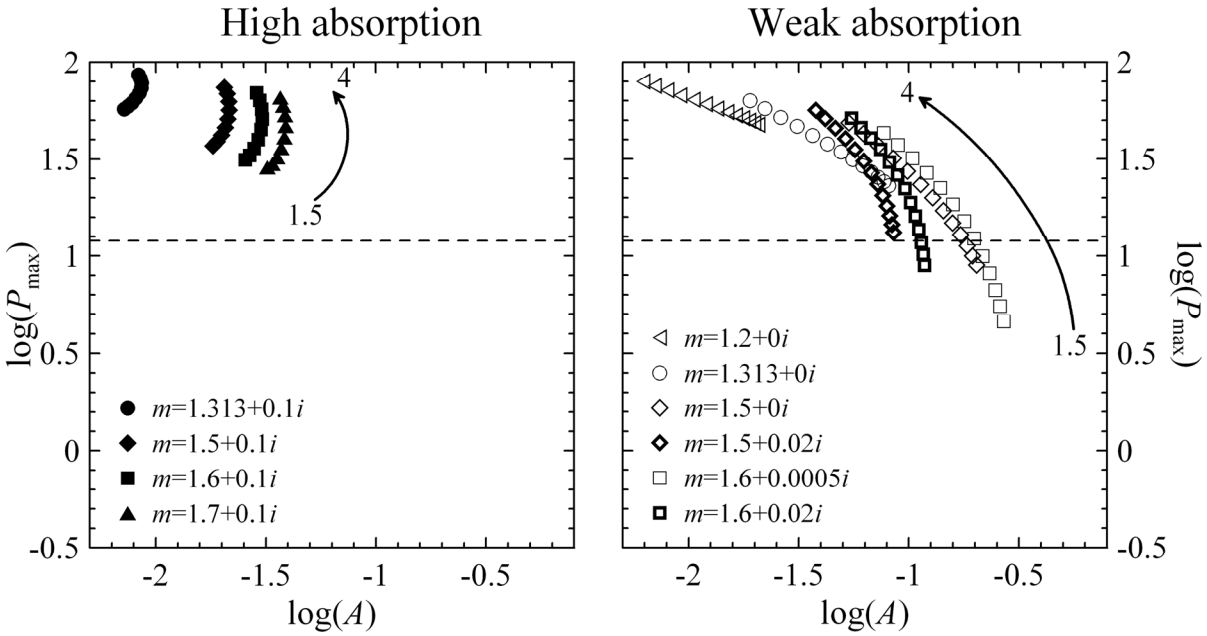
High absorption
Weak absorption
log(P_{max})
log(A)
4
1.5
m=1.313+0.1i
m=1.5+0.1i
m=1.6+0.1i
m=1.7+0.1i
m=1.2+0i
m=1.313+0i
m=1.5+0i
m=1.5+0.02i
m=1.6+0.0005i
m=1.6+0.02i

Fig. 6.

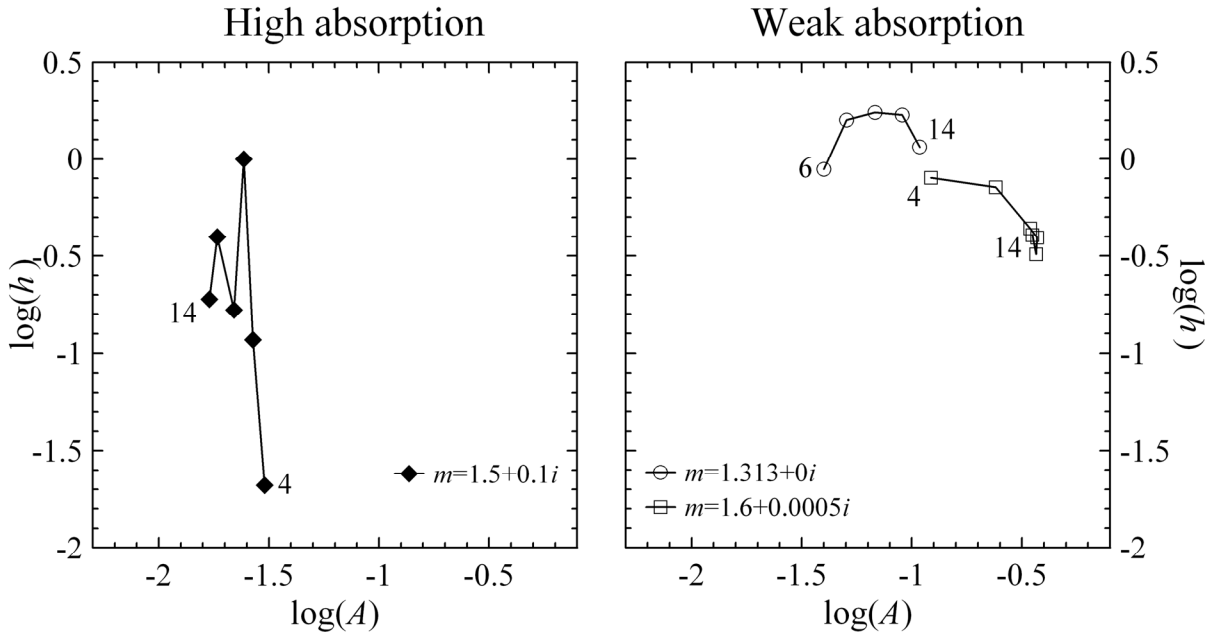
High absorption
Weak absorption
log(h)
log(A)
m=1.5+0.1i
m=1.313+0i
m=1.6+0.0005i
14
4
6

Fig. 7.